Study of metal–ceramic WC/Cu nano-wear behavior and strengthening mechanism

Min Zheng(郑敏)[1], Jie Chen(陈杰)[1], Zong-Xiao Zhu(朱宗孝)[1,†], Ding-Feng Qu(曲定峰)[1], Wei-Hua Chen(陈卫华)[1], Zhuo Wu(吴卓)[1], Lin-Jun Wang(王林军)[1], and Xue-Zhong Ma(马学忠)[2]

[1] *School of Mechanical and Electrical Engineering, Lanzhou University of Technology, Lanzhou* 730050, *China*
[2] *School of Petroleum and Chemical Engineering, Lanzhou University of Technology, Lanzhou* 730050, *China*

(Received 24 May 2022; revised manuscript received 24 August 2022; accepted manuscript online 2 September 2022)

In view of the inherent poor tribological properties of copper, the reinforcement of copper matrix composites with WC particles presents a promising research area with significant industrial influence. Therefore, in the present study, a molecular dynamics approach is used to simulate the process of repeated friction of diamond grinding balls on WC/Cu composites, and the friction force, friction coefficient, abrasion depth, wear rate, abrasion morphology, von-Mises stress, internal defects, workpiece energy, and performance comparison of different layer thicknesses are systematically investigated in the multiple friction process. It is found that the fluctuation amplitude of friction force, friction coefficient, and abrasion depth are smaller and the fluctuation frequency is larger during the initial friction, whereas near the WC phase, there appears extreme values of the above parameters and the von-Mises stress is highly concentrated while the workpiece energy contonues to increase. In the case of the repeated friction, with the increase of friction times, the friction force, friction coefficient, and abrasion depth fluctuation amplitude increase, the fluctuation frequency decreases, the workpiece energy reaches an extreme value near the WC phase, and a large number of dislocations plug, therefore, the region is strengthened. As the distance between the grinding ball and the WC phase decreases, the more obvious the strengthening effect, the stronger the ability of workpiece to resist the wear will be.

Keywords: molecular dynamics, repetitive friction, copper matrix composites, reinforcement

PACS: 68.35.bd, 31.15.at, 46.55.+d, 81.05.Mh **DOI:** 10.1088/1674-1056/ac8ea0

1. Introduction

Tribology is a subject that studies the friction, wear, and lubrication of interacting surfaces. Wear is an essential field of tribology, and has a significant influence on the lifetime of mechanical components from a nanoscale to a macro scale, which is a lasting phenomenon of deformation, damage, or removal of materials on contacting surfaces.[1] According to statistics, approximately 23% of the energy consumption in the world came from tribological contact, of which 20% is used to overcome friction and 3% is spent on remanufacence worn parts and spare equipment due to wear and wear-related failures.[2] With its excellent plasticity, toughness with ductility, and corrosion resistance, copper matrix composites have been widely used in various fields such as automotive, rail transportation, machinery manufacturing, defense industry, and aerospace.[3,4] In recent years, with the accelerating development of modern industrial technology, higher requirements for the mechanical properties of copper matrix composites have been put forward. Copper matrix composites with Cu serving the matrix, after a certain quantity of reinforcements has been added, can break through the limitations of a single metal or alloy matrix to give excellent mechanical properties, wear resistance, and corrosion resistance,[5–8] in particular, the copper matrix composites doped with carbide phase integrates many excellent properties of ceramic and copper matrix materials in unity.[9] The high melting point, high hardness and load-bearing capacity of metal–ceramic WC particles can make them better withstand wear with reduced volume loss during frictional wear of WC/Cu composites, which are widely used in the preparation of anti-wear materials under harsh conditions.[10,11] Mechanical components, manufacturing tools, and most engineering systems (whose mating parts are in relative motion) can face serious failures due to the frictional wear resulting in significant energy dissipation, thereby making the study of frictional wear of copper matrix composites greatly important.

Molecular dynamics (MD) simulations as a scientific algorithm have proven to be a powerful tool for studying physicochemical changes in materials at a microscopic level.[12–14] Shabani *et al.*[15] investigated the effects of SiC particles and the preparation method on the tribological properties of pure Cu and SiC/Cu composites by dry sliding wear tests. It was reported that the lowest wear loss is observed for the sintered forged Cu composite compacts with 60% SiC content. Wei *et al.*[16] prepared graphene/Cu-based (Gr/Cu) composite foils by pulsed electrodeposition and characterized their morphology, microstructure, tensile properties, and nanoindentation hardness. The obtained results showed that the variances in tensile strength and hardness are mainly attributed to

†Corresponding author. E-mail: zhuzongxiaolut@163.com

© 2023 Chinese Physical Society and IOP Publishing Ltd

the variation in grain size. Freschi *et al.*[17] experimentally investigated the micro and nano WS_2 structures to improve the tribological properties of copper matrix composites. Li *et al.*[18] investigated the effect of different spatial structures of ball-milled graphene/copper powders on the microstructure and mechanical properties of the composites. It was demonstrated that the yield strength and tensile strength of graphene-copper matrix composites are increased by 136.6% and 16.7%, respectively, while elongation is maintained at 35.2% compared with pure copper. Chen *et al.*[19] prepared gradient-distributed SACNT/Cu composites as well as SACNT films covered with electroplated copper layers by electrodeposition. It was found that the stress and strain hardening from dislocation stacking are responsible for their superior mechanical properties. Bahador *et al.*[20] prepared Cu-8wt% TiO_2 composites with different holding times by using a hot extrusion process and investigated the synergistic strengthening mechanism of nano-TiO_2 and copper matrix composites. It was noted that uniformly distributed reinforcing particles and grain refinement triggered both strengthening and ductility enhancement. Zhang *et al.*[21] designed several graphene/copper nanocomposites and investigated their compressive behavior by molecular dynamics simulations. By reducing the twin spacing and introducing multiple layers of graphene, they found that the interaction between graphene and copper nano matrix can be enhanced. Song *et al.*[22] investigated the effect of the amorphous phase CuZr on the plastic deformation behavior of nano-polycrystalline Cu by using molecular dynamics simulations. It was demonstrated that the introduction of the amorphous phase can effectively improve the plasticity of nano-polycrystalline Cu due to the synergistic effect between the amorphous and crystalline phases. Peng *et al.*[23] investigated the strengthening mechanism of graphene coatings on copper film substrates by molecular dynamics simulations of nanoindentation. In the study, it was found that the load-bearing capacity of the copper substrate is significantly increased after graphene coating coverage, which is proportional to the number of layers of graphene from single to triple layers. Feng *et al.*[24] revealed the deformation characteristics and plasticity mechanism of WC–Co composites through molecular dynamics simulations. Then, it was found that the nucleation, expansion, and interaction of dislocations substantially depend on the loading direction. Zhu *et al.*[25] investigated the strengthening effect of graphene blocking dislocation propagation in graphene-reinforced copper matrix composites by MD simulations. Sequentially, it was found that the strengthening effect of graphene can be improved by adjusting the angle and arrangement of graphene.

In the comprehensive researches of copper matrix composites on a microscopic scale, there remain numerous topics to be studied, in particular, repeated friction studies on the surface of the workpiece have not been carried out, and the microscopic reinforcement effect of the particle reinforcement on the copper matrix, the repeated friction of copper matrix composites friction and wear phenomenon are still unclear. By building a molecular dynamics model of copper matrix composites containing WC particles for reinforcements and simulating the frictional wear behavior under repeated friction according to the actual working conditions, and investigating the strengthening effect of the metal–ceramic WC on the copper matrix from various aspects, the present paper lays an extensive foundation for microscopic study of the effect of particle reinforcements on the matrix.

2. Computation and modeling

2.1. Friction modeling and simulation process

The conventional friction test principle is illustrated in Fig. 1, where the pallet is used to support the workpiece substrate, the fixture serves as loading the workpiece, the pressure plate as holding the workpiece, and the thermocouple is utilized to adjust the test temperature, in addition, a constant load is used to implement the counterweight balance. The pallet, fixture, workpiece, and press piece are combined into one component of rotational motion, where ω denotes the rotational angular velocity, and the grinding ball is welded to the connecting rod to apply a constant load through a counterweight.

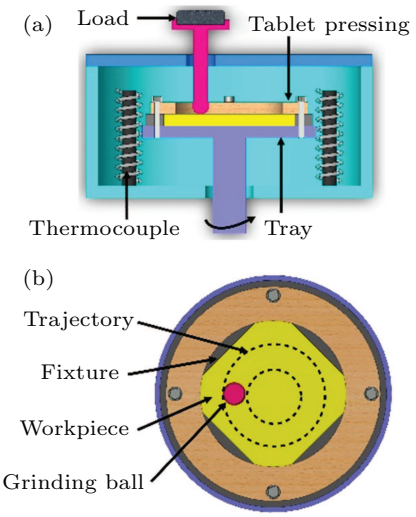


Fig. 1. Schematic diagram of friction test.

For this simulation, the metal–ceramic WC/Cu phase microscopic wear strengthening mechanism is investigated by combining the above friction principle and molecular dynamics simulation method. The simulation model consists of two parts as shown in Fig. 2: one is a diamond grinding ball and the other is a WC/Cu composite. The emphasis in this paper is placed on the effect of the presence of the cermet WC on the matrix Cu, furthermore, the hardness of the diamond grinding ball is much higher than that of the WC/Cu composite, so

the grinding ball under reasonable assumptions is considered as a rigid body. As shown in Fig. 2(a), the purple rectangle represents the workpiece, the red ball refers to the diamond grinding ball, the red arrow is the direction of the grinding ball movement, the yellow dotted circular ring denotes the grinding ball movement trajectory, the four black dashed circles represents the reinforced phase WC phase distribution positions, and R is the rotational friction radius. To prevent van der Waals forces from appearing between the atoms of the grinding ball and the substrate, the initial position of the grinding ball is set to 20 Å away from the upper surface of the substrate, which is far greater than the free range between the grinding ball and the workpiece, to ensure the accuracy of the simulation. The workpiece shown in Fig. 2(b) consists of three layers, *i.e.*, boundary layer, thermostatic layer, and Newtonian layer. The boundary layer always keeps the atoms fixed, *i.e.*, subjected to no atomic vibrations, maintains periodic boundary conditions along the x and y directions, and free boundary conditions in the z direction to eliminate boundary effects; the constant temperature layer is utilized to keep the system temperature constant; the Newtonian layer is the focus of microfriction and wear research, and it satisfies Newton's second law of motion.[26–28] The conjugate gradient method has been used for energy minimization in the relaxation process to eliminate unreasonable factors for model building, such as atomic overlap.[29]

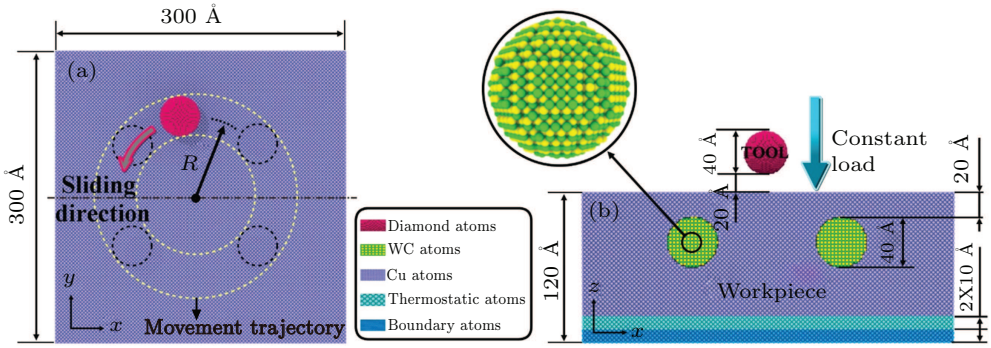


Fig. 2. Geometrical characteristics of WC/Cu sample of (a) front view and (b) top view.

Table 1 lists the parameters chosen for the simulation in this work. The dimensions of the workpiece are 30 nm×30 nm×12 nm, containing 923824 atoms, with a grinding ball radius of 2 nm, containing 5955 atoms. In this work, the Verlet algorithm is chosen for MD simulations in time steps of 1 fs and an initial temperature is set to 300 K.[30] The grinding ball moves circularly at a constant linear velocity of 1.6×10^{-3} Å/fs and a constant load of 60 nN, with a rotation radius of 8.5 nm.

Table 1. Calculation parameters for MD friction simulations.

Materials	Workpiece	Tool: Diamond
Dimensions	Cubic: 30 nm×30 nm×12 nm	Spherical: $R = 2$ nm
Atomic number	923824	5955
Interatomic potential	Morse EAM Tersoff	Morse
Time step	1 fs	
Initial temperature	300 K	
Grinding velocity	1.6×10^{-3} Å/fs	
Normal load	60 nN	
Grinding radius	8.5 nm	

2.2. Selection of potential function

The choice of potential function is particularly critical to the accuracy and precision of molecular dynamics simulation calculations. In this work, Morse potential (Morse), embedded atom potential (EAM potential), and Tersoff potential are used to describe the interactions between different atoms.

Morse potential refers to a simple model that can simulate the potential energy of interaction between metal atoms and other atoms, which is widely used in the simulation of molecular dynamics of metal tool grinding.[31] In this work, Morse potential is used to describe the force between C atom of tool, and W atom of strengthening phase, C atom of tool, C atom of tool and Cu atom of matrix, C atom of strengthening phase and Cu atom of matrix, which is specifically shown below:[32]

$$\alpha U_{\text{Morse}}(r_{ij}) = D\left[\mathrm{e}^{-2(r_{ij}-r_0)} - 2\mathrm{e}^{-\alpha(r_{ij}-r_0)}\right], \qquad (1)$$

where D is the cohesive energy of the interaction, r_0 and r_{ij} are the equilibrium distance and separation distance between atoms i and j, respectively, and α is the bulk modulus fitted to the material. The parameters are shown in Table 2.

Table 2. Parameter settings of Morse potential function.[33,34]

Atomic type	D_0 (eV)	α (Å^{-1})	r_0 (Å)
C–W	6.64	1.80370	1.90547
C–C	6.0	2.1	1.39
C–Cu	0.087	1.7	2.2

The EAM potential function is a typical many-body potential applicable to metal-atom systems, which can describe the interaction between metal atoms more accurately. The EAM potential describes the interaction forces between Cu–Cu, W–Cu, and W–W in this paper, with their expressions

shown in Eqs. (2) and (3)[35–37] and some of fitting parameters used here are shown in Table 3:

$$E_{\rm tot} = \frac{1}{2}\sum_{ij}\phi_{ij}(r_{ij})\sum_{i}F_i(\rho_i), \tag{2}$$

$$\rho_i = \sum_{j\neq i}\rho_j(r_{ij}), \tag{3}$$

where F_i is the embedded potential energy of atom i, ρ_i is the electron cloud density of other atoms, ϕ_{ij} is the pair potential between atoms, r_{ij} is the distance between atoms, and ρ_j is a function of the electron cloud density.

Table 3. Fitting parameters for Cu–Cu, W–W, and Cu–W potentials.[38]

Cu–Cu		W–W		Cu–W	
χ	11.13411	χ	6.180475	A	0.566522
α (eV)	0.72840	k_0 (eV)	–0.581958		
β	3.45096	k_1 (eV)	–2.175059	B (Å)	0.495555
$r_{\rm a}$ (Å)	1.62684	k_2 (eV)	17.053662		
F_1 (eV)	0.67648	k_3 (eV)	–8.215139	C (Å)	0.083299
$r_{\rm s}$ (Å)	3.696	$r_{\rm s}$ (Å)	3.236		
$r_{\rm c}$ (Å)	4.102	$r_{\rm c}$ (Å)	3.592		
n	0.33333	n	0.44		

Using the Tersoff potential to describe the interaction between carbon and tungsten atoms in the reinforcing phase WC, and the reinforcing phases C–C and W–W atoms, the expressions are shown in Eqs. (4) and (5),[33,39] and some of the parameters used for fitting are shown in Table 4:

$$E = \frac{1}{2}\sum_{i}\sum_{j\neq 1}V_{ij}, \tag{4}$$

$$V_{ij} = f_{\rm c}(r_{ij})[f_{\rm R}(r_{ij}) + b_{ij}F_{\rm A}(r_{ij})], \tag{5}$$

where V_{ij} is the potential energy between atoms, $f_{\rm c}(r_{ij})$ the phase radius, $f_{\rm R}(r_{ij})$ the pair potential of mutual attraction between atoms, b_{ij} the modulation function , and r_{ij} the atomic spacing.

Table 4. Main parameters for fitting Tersoff potential function.[33]

Parameter	C–W	C–C	W–W
D_0 (eV)	6.64	6.0	5.41861
r (Å)	1.90547	1.39	2.34095
β (Å^{-1})	1.80370	2.1	1.38528
S	2.96149	1.22	1.92708
γ	7.2855×10^{-2}	2.0813×10^{-4}	1.88227×10^{-3}
c	1.10304	330.0	2.14969
d	0.33018	3.5	0.17126
h	0.75107	1.0	–0.27780
R (Å)	2.80	1.85	3.50
D (Å)	0.20	0.15	0.30

3. Results and discussion

3.1. Effect of friction on mechanical properties of workpiece and shape of abrasion marks

For investigating the effect of the grinding ball on the friction force during repeated friction, the force on the workpiece in x, y, and z directions are extracted as shown in Fig. 3. It can be seen that the component force in the x and y directions are periodically distributed in the form of sine and cosine function, respectively, which can be attributed to the fact that the grinding ball moves circularly and its motion determines the distribution pattern of the x and y directional forces when the x directional force is 0 (*e.g.*, point L in Fig. 3), the y directional force reaches its peak (*e.g.* point H in Fig. 3). Meanwhile, the z-directional force increases rapidly to the point at the initial friction and then fluctuates up and down around a fixed value. This is attributed to the fact that the grinding ball starts as a downward pressure process and the workpiece undergoes elastic deformation, resulting in a continuous increase in the force in the direction of F_z. Afterward, it enters into a stable friction phase, always fluctuating up and down around a fixed value, which is caused by the constant downward force exerted on the grinding ball. b, c, and d represent the peak values of F_x in the initial, secondary, and tertiary frictions, respectively. It can be seen that the value of b is greater than the that of c and d. Owing to the initial friction, the grinding ball releases more atoms of abrasive chips, which cause the workpiece to produce a larger resistance.

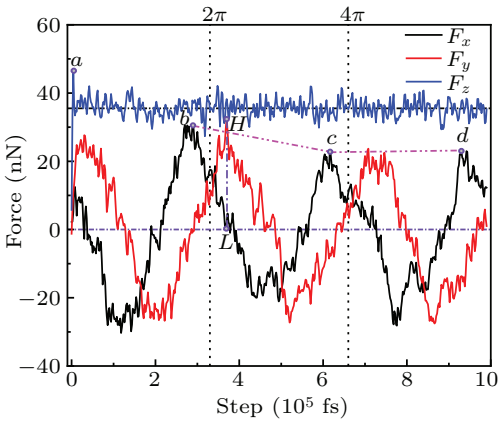


Fig. 3. Interaction between grinding ball and workpiece in x, y, and z directions.

To further study the law between the influence of friction fluctuation and material deformation accurately, the x- and y-directional components are combined to obtain a friction force, which is given by

$$F_{\rm f} = \sqrt{(F_x)^2 + (F_y)^2}, \tag{6}$$

where is the frictional force, F_x the x-directional force, and F_y the y-directional force.

The dynamic response curve of $F_{\rm f}$ *versus* time step is shown in Fig. 4, where I is the initial friction phase and II is the repeated friction phase. By observation, it is found that increases rapidly from 0 during the initial friction, and then stabilizes around a fixed value with small fluctuations, averaging 24.58 nN. Entering into the repeated friction phase, the curve fluctuates sharply, moreover, the peak appears near the

WC phase and the trough occurs far from the reinforced phase, and the average value of this phase is 20.04 nN, which is much smaller than the average value of the initial friction. In addition, at the same position, it is found that the difference between the peak value and valley value of the third friction is greater than the difference between the peak value and valley value of the second friction, *i.e.*, $\Delta h_2 > \Delta h_1$, as shown in Fig. 4. This is attributed to the fact that the closer to each other the grinding balls in the WC phase as the friction increases, the more noticeable the effect of WC relative to the matrix Cu.

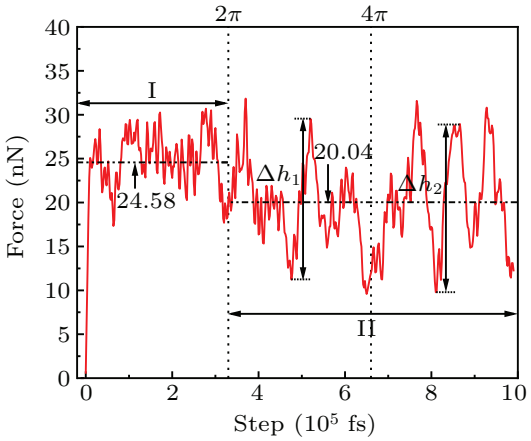


Fig. 4. Dynamic response curve of friction *versus* time step.

The coefficient of friction represents the ratio of the frictional force between two surfaces to the normal force acting on one of them, reflecting the frictional properties of the material, whose expression is shown below:[40]

$$\mu = F_{\mathrm{f}}/F_z, \tag{7}$$

where μ is the friction coefficient, F_{f} the combined friction force, and F_z the normal force.

The dynamic response curve of the friction coefficient *versus* time step is shown in Fig. 5, indicating that the variation of the friction coefficient also shows two stages with different characteristics. In the initial friction stage I, the friction coefficient increases rapidly from 0, and then fluctuates above and below a fixed value, with an average friction coefficient of 1.4436. This is attributed to the better flatness of the workpiece surface during the initial friction, meanwhile, the distance between the grinding ball and WC phase is large, with the WC having no significant action relative to the substrate Cu, making the fluctuation of the friction coefficient relatively gentle. In the repetitive friction phase II, the alternation of the curve crest and trough is more intense, and the average friction coefficient is 1.9223, which arises from the increase in the roughness of the friction on the surface with the increase of the number of friction, in addition, smaller distance between the grinding ball and the WC phase, making the average friction coefficient gradually increase, therefore, the difference between the crest and trough becomes more and more obvious.

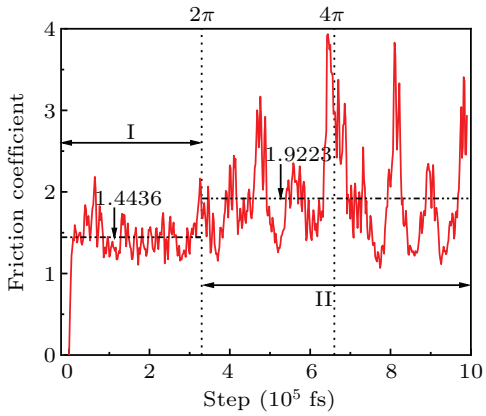


Fig. 5. Dynamic response curve of friction coefficient *versus* time step.

To investigate the variation of the abrasion depth, the workpiece z-directional height is color-calibrated as shown in Fig. 6, where blue is the deepest abrasion mark, and red is the shallowest abrasion mark, with the black dashed ellipse marking the deepest abrasion mark during each friction circle. To investigate the variation of the abrasion depth, the workpiece z-directional height is color-calibrated as shown in Fig. 6, where blue is the deepest abrasion mark, red is the shallowest abrasion mark, and the black dashed ellipse is the deepest abrasion mark during each friction circle. When the grinding ball grinds through the center of the WC phase, the grinding depth starts to deepen, but when the grinding ball moves to the front end of the WC phase, the depth of the friction marks is the shallowest. This results from the WC phase causing the workpiece atoms driven by the grinding ball motion to be blocked at its front end. However, after the grinding ball has ground through the WC phase, the grinding ball only acts on the single crystal copper and the material is removed relatively easily, ultimately resulting in a difference in material removal. In the repeated friction phase, the above phenomenon becomes more and more obvious. As shown in Figs. 6(b) and 6(c), in the front end of the WC phase, there is no blue area, but at the back end of the WC phase, there are more and more blue area, and their areas become larger and larger. It shows that the presence of the WC phase makes the friction surface depth gap larger and larger with the increase of friction times.

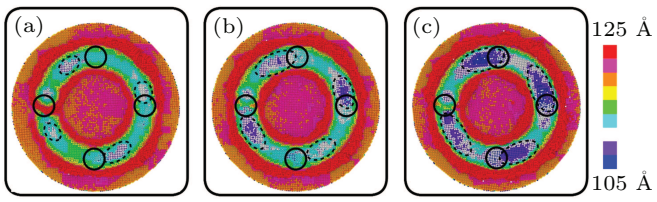


Fig. 6. Nephogram of depth distribution of wear marks in three circles of workpiece.

Figure 7 shows the analysis of the real-time abrasion depth data in the whole friction process, revealing that the fluctuation of abrasion depth is small during the initial friction,

nevertheless, the fluctuation frequency is larger, and when the friction is repeated, the fluctuation frequency decreases gradually, whereas the fluctuation amplitude gradually increases. This is because in the initial rubbing process, the surface of the workpiece is flatter, therefore the change of the wave crest and trough becomes more gentle. However, the internal deformation of the intact workpiece is more violent during the initial friction, resulting in a faster frequency of change in the depth of the abrasion marks. In the three rubbing processes, the difference between the second wave crest and the wave trough grinding marks respectively are $\Delta h_1 = 2.36482$ Å, $\Delta h_2 = 4.71513$ Å, and $\Delta h_3 = 7.17584$ Å. It is evident that $\Delta h_1 < \Delta h_2 < \Delta h_3$, *i.e.*, the difference between the wave crest and the wave trough becomes larger as the friction increases. The reason for this phenomenon is that the smaller the distance between the grinding ball and the WC phase, the more obvious the strengthening effect of WC than that of the matrix Cu.

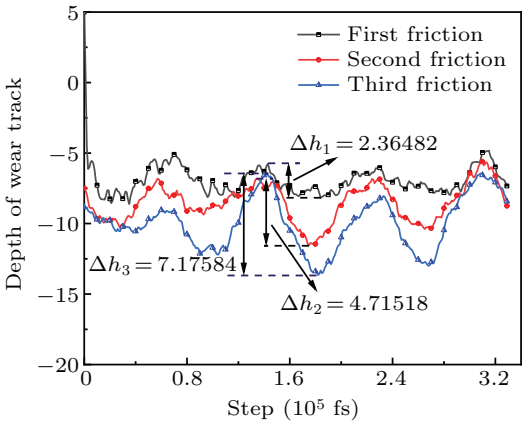


Fig. 7. Dynamic variation curve of wear mark depth *versus* time step.

The wear rate refers to an important measure of material stiffness, which can be calculated by the wear chip volume during the friction process. Figure 8 shows a schematic diagram of three frictional wears. In these three frictional processes, none of the depths of the abrasion marks exceeds the radius of the grinding ball, so only the case where the depth of the abrasion marks does not exceed the radius of the grinding ball is considered in the calculation of the chip volume. According to the instantaneous abrasion depth Δh, the instantaneous grinding chip volume ΔV can be calculated, and the formula is

$$\Delta V = \frac{\pi}{3}(3R - \Delta h)(\Delta h)^2, \tag{8}$$

where ΔV is the instantaneous grinding chip volume, Δh the instantaneous grinding mark depth, and R the grinding ball radius.

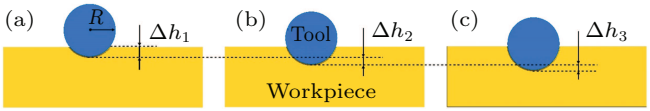


Fig. 8. Schematic diagram of friction process.

For homogeneous materials, the relationship of abrasive chip volume ΔV, with the sliding distance L and the normal load F at the contact point is described as the Archard equation as follows:[41]

$$\Delta V = \vartheta F L, \tag{9}$$

where ϑ is the instantaneous wear rate and is the instantaneous wear volume, L is the sliding distance, and F is the normal load at the contact point. Thereby the formula for calculating the instantaneous wear rate is obtained as follows:

$$\vartheta = \frac{\Delta V}{FL}. \tag{10}$$

The dynamic response curve of the wear rate against time step is shown in Fig. 9. It can be seen that the curve fluctuates greatly during the initial friction, the peak position appears at the position without the WC phase, the trough position appears near the WC phase,and the average wear rate is relatively large with a value of 0.1503 nm^3/nN·nm. For the initial friction, the distance between friction surface and WC phase is larger, thereby making it easier to remove the workpiece material. In the process of repeated friction, the average wear rate decreases rapidly as the number of friction increases, with a wear rate of 0.0124 nm^3/nN·nm for secondary friction and 0.0097 nm^3/nN·nm for tertiary friction, respectively, which is because of repeated friction leading to friction hardening on the surface of the abrasion marks and the weakened ability of the grinding ball to remove material. The wear rate curve more fully illustrates that the existence of the WC phase has a certain enhancement effect on the matrix Cu, in addition, when the distance between the grinding ball and the WC phase is smaller, the effect of the enhancement of the WC phase on the matrix Cu is more obvious. Khosravi *et al.*[42] prepared WC/Cu composites by friction stirring process and the results showed that the microhardness of WC/Cu composites increases up to twice that of pure copper, which is in agreement with the one we reached.

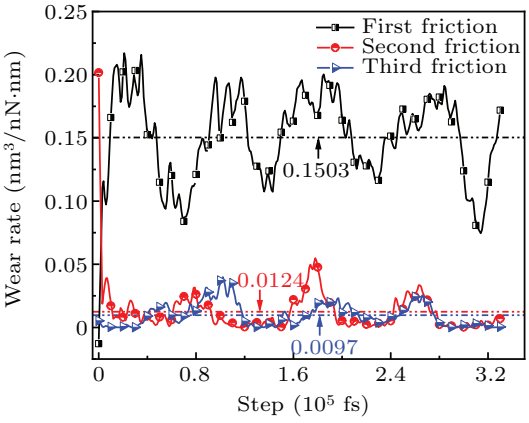


Fig. 9. Dynamic change curve of wear rateversus time step

To observe the stress distribution in the Cu/WC workpiece, the stresses are calculated by using von-Mises and the expression is shown below:[43]

$$\sigma_{\mathrm{M}} = \sqrt{\frac{1}{2}\left[(\sigma_{xx}-\sigma_{yy})^2+(\sigma_{xx}-\sigma_{zz})^2+(\sigma_{yy}-\sigma_{zz})^2\right]+3\left(\sigma_{xy}^2+\sigma_{yz}^2+\sigma_{xz}^2\right)}, \tag{11}$$

where σ_{xx}, σ_{yy}, and σ_{zz} are all-directional positive stresses, σ_{xy}, σ_{yz}, and σ_{xz} are all-directional tangential stresses.

Von-Mises stress distribution in the friction process is shown in Fig. 10. During the initial friction, the von-Mises stress distribution of grinding balls passing through the second WC ball and the third WC ball are shown in Figs. 10(a) and 10(b), while that passing through the substrate Cu is shown in Fig. 10(c). It can be seen that the local stresses are larger and highly concentrated when the grinding ball moves to the front end of the WC phase, whereas the local stresses are smaller and dispersed when the grinding ball only acts on the matrix Cu.

Figures 10(e)–10(g) show the von-Mises stress distributions at the same position during the first friction, second friction, and third friction, respectively. It is observed that the area of the red region increases with the increase of the number of friction turns as well, and it is always distributed near the WC phase, indicating that the distance between the grinding ball and the WC phase gradually decreases with the increase of the friction times, and the von-Mises stress near the WC phase gradually increases.

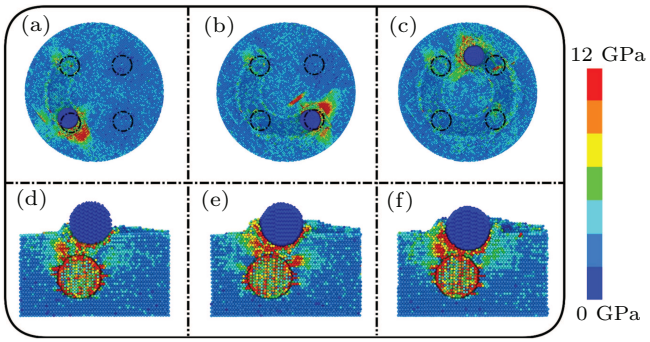


Fig. 10. Stress distribution diagram of friction processes.

3.2. Variation of workpiece debris atoms, internal defects, and energy with friction process

To investigate the distribution of abrasive chips generated by the grinding ball during the motion, color calibration of the workpiece in the z-direction height is made, with the red position having the most abrasive chip accumulation and the blue position having the least abrasive chip accumulation, as shown in Fig. 11. As can be seen, at the first friction, near the WC phase, fewer abrasive chips accumulate, whereas, in the absence of the WC phase, more abrasive chips accumulate, with the increase in the number of friction turns, this phenomenon becomes more obvious. The reason for this is that when the grinding ball moves near the WC phase, the action of the WC phase causes relatively less material to be removed by friction, and the formation of chips is successively reduced. However, when the grinding ball moves to the position where only the matrix Cu is present, the lack of the WC phase causes relatively more material to be removed during the friction and relatively more chips to be formed. This phenomenon indicates that the existence of the WC phase makes it difficult to remove the nearby material, and the removal of abrasive chips is discontinuous.

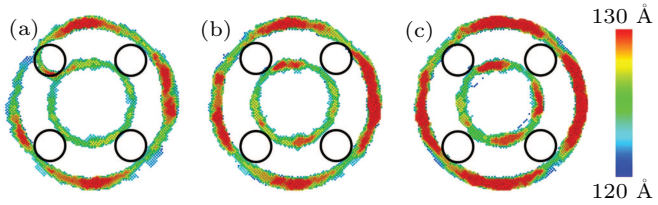


Fig. 11. Atomic number distributions of debris in the friction processes.

To further investigate the distribution of the debris atoms, the number of debris atoms in the inner ring and outer ring at the location with and without the WC phase in the three friction processes are counted and the results are shown in Fig. 12. As can be seen, in the initial friction process, the increase in the number of debris atoms grows faster and the number of debris atoms is much more, while in the repeated friction process, the increase in the number of debris atoms slows down rapidly and the number of debris atoms is less. Meanwhile, the slope of the curve is smaller when the grinding ball moves near the WC phase, the slope of the curve has a larger slope when it moves to the matrix Cu.

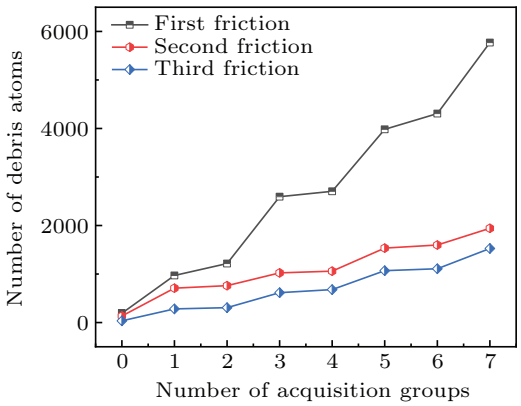


Fig. 12. Plots of number of debris atoms *versus* number of acquisition groups near strengthened and non-strengthened phases.

To further investigate the variation of the atomic number of internal defects in the three friction sessions, the atomic number of some defects is counted, and the results are shown in Fig. 13. Figure 13(a) shows the dynamic response curves of the number of atoms generating HCP and BCC defects *versus* time stepin the three friction sessions. The blue curve presents the curve obtained by polynomial fitting of the HCP curve, which shows that the number of HCP increases throughout the

friction process, and the increasing rate gradually slows down with the increase of the friction times. This is because in the initial friction process, the grinding ball gives rise to continuous extrusion on the workpiece, resulting in severe plastic deformation. A large amount of energy is accumulated in the workpiece, which is released in the form of defects or dislocations, resulting in the change of grain structure, which leads a large number of FCC atoms to transform into HCP, which is a common phase transformation of FCC crystals. The extrusion of diamond grinding ball causes the distance between the atoms in deformation zone to decrease, resulting in the formation of HCP structure, that is, the elastic–plastic deformation in the deformation zone. However, during repeated friction, the surface of the workpiece after the initial friction is destroyed, resulting in a slowdown in the growth rate of the atomic number of the HCP structure. The number of atoms of the BCC structure increases rapidly from 0 to a maximum value under the initial frictional grinding ball downward pressure, stabilizing during the subsequent friction.

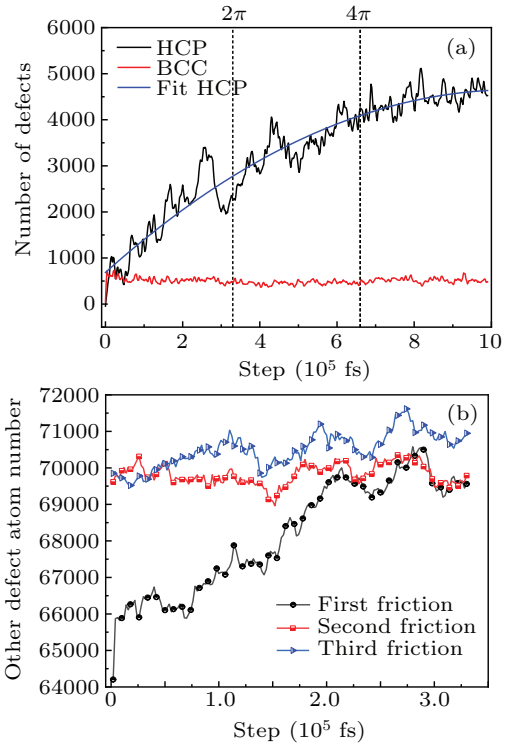


Fig. 13. Dynamic response curves of atomic number of internal defects *versus* time step.

Figure 13(b) shows the dynamic response curves of the number of amorphous atoms *versus* time step in the three friction processes. In the initial friction process, the atomic number of other structures, rises rapidly, which is attributed to a large number of debris atoms generated in the initial friction process on the one hand, and the intense plastic deformation on the other hand, which generates a large number of dislocations. However, during repeated friction, the distance of the grinding ball relative to the WC phase decreases, resulting in the weakening of the ability of the grinding ball to remove material due to the WC phase and a decrease in the atomic number of chips produced, resulting in a stabilization of the growth rate of the atomic number of the other structure.

To better understand how the dislocations change in the friction process, the dislocation extraction algorithm (DXA) is used to identify the dislocations.[44] Previous studies have demonstrated that for single crystal materials with embedded inclusions, the semi-coherent interfaces form between them when the lattice mismatch exceeds 5%.[45] This phenomenon also occurs in the WC/Cu matrix, where the lattice mismatch reaches 24%. The lattice mismatch is calculated from the following equation:

$$k = \frac{a_{\mathrm{N}} - a_{\mathrm{S}}}{a_{\mathrm{N}}}, \tag{12}$$

where a_{N} is the lattice constant of WC, a_{S} the lattice constant of Cu, and k the lattice mismatch ratio.

Figures 14(a)–14(c) respectively show the dislocation distribution inside the workpiece when the grinding ball acts only on the substrate Cu in the three friction processes. Figures 14(d)–14(f) respectively show the dislocation distribution inside the workpiece when the grinding ball acts directly above the WC phase in the three friction processes. It is evident that the dislocation reaction is less when the grinding ball acts only on the matrix Cu, and however, the dislocation reaction is more when the grinding ball acts directly above the WC phase, which leads to an increase in the required friction force, a relatively small material removal when being frictionated under constant load, an increase in the friction coefficient, a shallow abrasion depth, and a highly concentrated stress distribution, which is also consistent with the results shown in Figs. 6, 10(a), and 10(b), indicating that the addition of WC particles leads to a significant increase in the wear resistance of the Cu-based composites. In addition, throughout the friction process, dislocations mainly accumulate between the grinding ball and the WC phase, and a small number of dislocations are attached to the surface of the WC phase in the unground region as shown in Fig. 14(a) in 1. As the friction increases, the dislocation density gradually increases both when the grinding ball acts on the substrate Cu and by pressing positively onto the WC phase directly above, but the dislocation density directly above the WC phase is significantly larger than that when the grinding ball acts on the substrate Cu as shown in Fig. 14(c) in 3 and Fig. 14(f) in 3′. This is due to the stress concentration between the grinding ball and WC phase when the grinding ball moves near the WC phase, which is easy to produce a large number of dislocations, and the sliding of dislocations is blocked by the WC phase, forming dislocation plugging and producing a high dislocation density region. At the same time, with the increase of friction times, the distance between the grinding ball and WC phase decreases, and the strengthening effect becomes increasingly obvious.

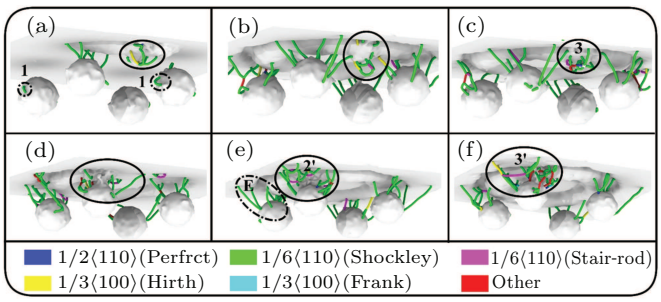


Fig. 14. Dislocation distributions at different positions, showing dislocation distributions in matrix when grinding ball is [(a)–(c)] far from WC and [(d)–(f)] near WC phase during three cycles of friction.

We also find that the dislocation forming between the ground WC phase and the friction surface reverts from agglomerated structural dislocations to straight lines when the grinding ball leaves the WC phase as shown with E in Fig. 14(e). In addition, some reactions occur between the new dislocations at the WC/Cu interface and the fixed dislocations, leading to the generation of Stair-rod dislocations and Hirth dislocations as shown in Fig. 14(e) in $2'$ and Fig. 14(f) in $3'$, with the interface transforming into a region containing high dislocation density. This phenomenon leads to the strengthening of the region — called Orovan strengthening.[46]

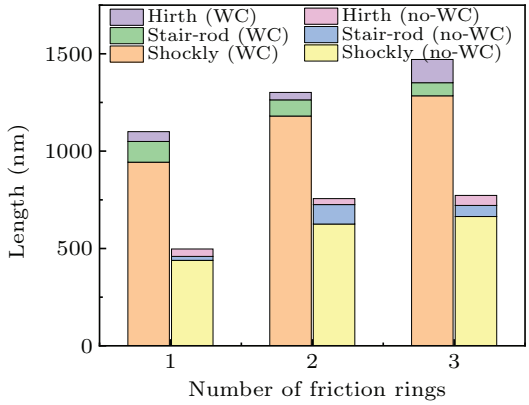


Fig. 15. Dislocation lengths *versus* different friction times steps.

For a clearer picture of the dislocation variation in the friction process, the lengths of Shockley, Stair-rod, and Hirth dislocations are calculated for each friction process when the grinding ball is located near the WC phase and when the grinding ball only acts on the substrate Cu as shown in Fig. 15. It is observed that in the whole friction process, the Shockley dislocations account for the largest length, and the total length of dislocations when the grinding ball moves near the WC phase is always larger than the total length of dislocations when the grinding ball only acts on the substrate Cu, meanwhile, the larger the number of friction, the longer the total length of dislocations is. This is attributed to the fact that Shockley dislocations control the plastic deformation of metallic materials throughout the deformation mechanism to such an extent that the internal deformation of the workpiece becomes more complex as the friction increases. In addition, there are a small number of Stair-rod dislocations and Hirth dislocations generated throughout the friction process, which are fixed dislocations that affect the deformation behavior by impeding the dislocation motion.[47]

Figure 16 shows the total number of various dislocations with the grinding ball located near the WC phase in the three friction processes *versus* number of friction times when the grinding ball only acts on the matrix Cu. It is observed that the total number of dislocations when the grinding ball is in the vicinity of the WC phase during each friction is always greater than the total number of dislocations when the grinding ball only acts on the matrix Cu, moreover, the total number of dislocations increases with the increase of friction, further verifying the strengthening effect of WCon the matrix as illustrated in Fig. 15.

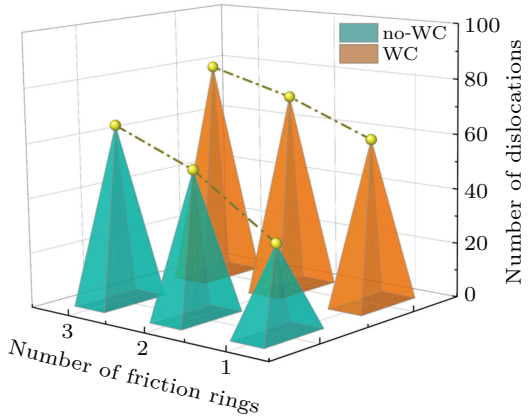


Fig. 16. Number of dislocations *versus* number of friction times steps.

Figure 17 shows the dynamic response curve of the total energy of the workpiece *versus* time step during the friction process. The change of the total energy of the workpiece is accompanied by the change of the atomic crystal structure, furthermore, the formation, migration, value-added, and annihilation of dislocations all cause the total energy of the workpiece to change. As can be observed from Fig. 17, the total atomic energy increases continuously during the initial friction. However, in the repeated friction phase, the growth speed of the total atomic energy tends to level off and there is a significant fluctuation, meanwhile, valleys appear near the WC phase as shown in Figs. 17(a)–17(d). This is attributed to the fact that during the initial friction, the larger the amount of material removed, the more the number of atoms undergoing lattice deformation is, and the strain energy accumulated in the lattice increases continuously, making the total energy increase continuously, while during repeated friction, the less the amount of material removed, the smaller the number of atoms undergoing lattice deformation is, and the change of strain energy

accumulated in the lattice tends to be flat. At the same time, the presence of valleys near the WC phase indicates numerous dislocations and defects forming near the WC phase, and the energy is consumed, resulting in energy values lying in the valleys.

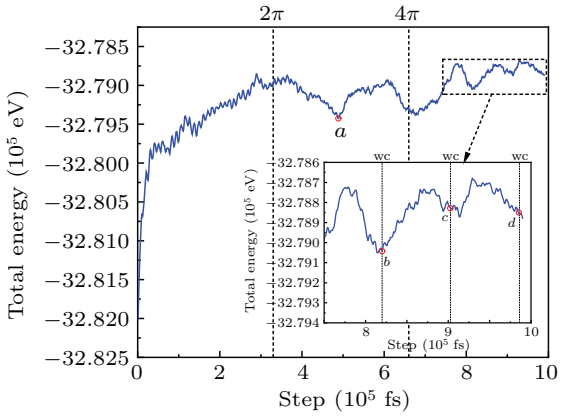


Fig. 17. Dynamic response curve of atomic energy of workpiece *versus* time steps.

3.3. Friction characteristics of WC phase at different distances from initial friction surface

To investigate the effects of different distances between the WC phase and the initial friction surface on the frictional wear behavior of the copper matrix composites, the friction is performed under different conditions of 20 Å, 25 Å, and 30 Å from the initial friction surface for the reinforced phase, respectively, and the dynamic response curves of the friction force *versus* time step under different conditions are shown in Fig. 18. As can be seen, the average frictional forces at different distances between the WC phase and the initial friction surface are 21.5597 nN, 18.7287 nN, and 17.8543 nN, respectively, with a smaller distance between the reinforced phase and the initial friction surface. The average frictional force is larger, and with distance increasing, the frictional force decreases. However, the difference between the average friction force at 20 Å from the initial friction surface and the average friction force at 25 Å from the reinforced phase is significantly larger than that at 25 Å from the initial friction surface and 30 Å from the reinforced phase. This indicates that the smaller the distance between the WC phase and the friction surface, the larger the average friction force is.

To further explore the friction performances of the WC phase and the initial friction surface at different distances, the dynamic response curves of the friction coefficients of the WC phase at different friction distances from the initial friction surface *versus* time step are plotted as shown in Fig. 19. It can be seen that when the WC phase is 20 Å from the initial friction surface, its friction coefficient fluctuates less during the initial friction, and when repeated friction, its friction coefficient fluctuation increases significantly, moreover, the peak appears at the front end of the grinding ball moving to the WC phase, and its average friction coefficient is 1.7621 in the whole friction process. However, when the WC phase is 25 Å and 30 Å from the initial friction surface, its friction coefficient fluctuates above and below a certain value throughout the friction process, with smaller fluctuations, and its average friction coefficient is 0.5229 and 0.4270 respectively throughout the friction process. From the average friction coefficient under different conditions, it can be seen that the strengthening degree of WC relative to the base copper has a certain range. When the WC phase is less than 20 Å from the workpiece surface, its strengthening effect is relatively obvious, and the strengthening effect is obviously weakened when the strengthening phase is greater than 20 Å from the initial friction surface, in addition, as the distance between the WC phase and the initial friction surface gradually increases, its strengthening effect gradually decreases until it disappears.

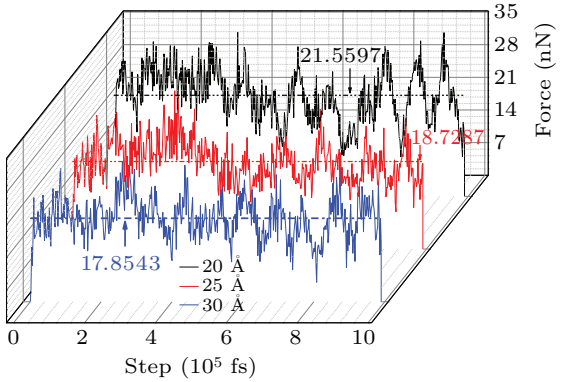


Fig. 18. Dynamic response curve of friction force *versus* time steps under different layer thicknesses.

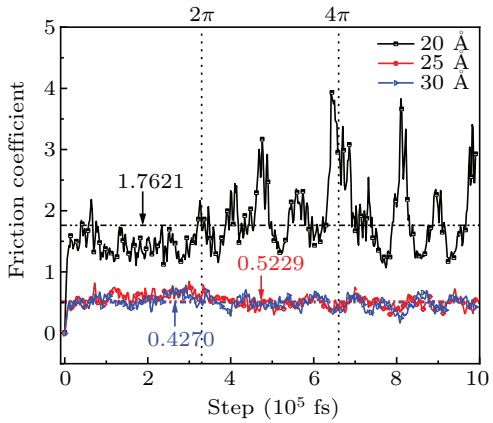


Fig. 19. Dynamic response curve of friction coefficient *versus* time steps under different layer thicknesses.

Figure 20 shows the dynamic response curves of the abrasion depth *versus* time steps for different layer thicknesses. It can be seen that the fluctuation amplitude of the abrasion depth is larger as the number of friction times steps increases when the WC phase is 20 Å from the initial friction surface. However, when the reinforced phase is 25 Å and 30 Å away from the initial friction surface, the fluctuation of the abrasion depth during the initial friction and the second friction are relatively

gentle, whereas a larger fluctuation occurs when entering into the third friction, with the peak position located near the WC phase. This demonstrates that the distance between the WC phase and the workpiece surface has a certain influence on the depth of the abrasion marks. When the distance between the WC phase and the workpiece surface is less than 20 Å, the strengthening effect of the WC phase on the substrate starts to appear, moreover, as the distance between the grinding ball and the WC phase decreases, the strengthening effect becomes more obvious.

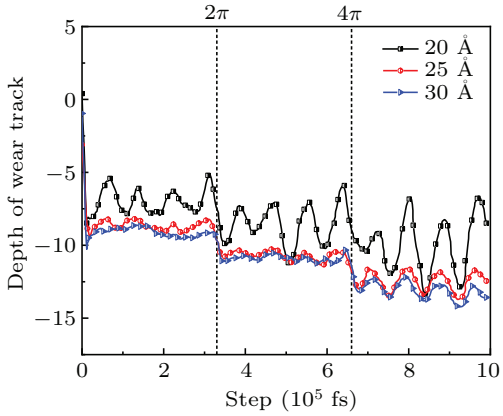


Fig. 20. Dynamic response curve of wear mark depth *versus* time steps for different layer thicknesses.

To accurately analyze the law of the distance between the WC phase and the friction surface related to the change of internal defect atoms during the friction process of the workpiece, the number of partial defect atoms generated inside the substrate in the friction process under different conditions is calculated. In the initial friction phase, the HCP atomic number increases faster at the distance of 20 Å from the friction surface in the WC phase, while entering into the repeated friction phase, the increase in the HCP atomic number gradually slows down, and the fluctuation frequency becomes more violent. However, when the WC phase is separately 25 Å and 30 Å away from the friction surface, the growth rate of HCP defect atomic number is relatively flat throughout the friction process, with the average HCP atomic number at 25 Å from the strengthening phase being slightly larger than that at 30 Å from the workpiece surface, but much smaller than the average HCP atomic number at 20 Å from the strengthening phase.

Figure 21(a) displays the dynamic response curves of the number of HCP defects *versus* time steps, and figure 21(b) shows those of the atomic number of other defects *versus* time steps for different conditions. During the initial friction phase, the increasing rates of other atoms under different conditions are all faster, while during the repeated friction phase, the increasing rates of other atoms tend to be smooth. However, the numbers of other atoms are produced when the distance between the WC phase and the initial friction surfaces are respectively 30 Å and 25 Å, which are significantly larger than the number of atoms produced when the distance between the WC phase and the initial friction surface is 20 Å.

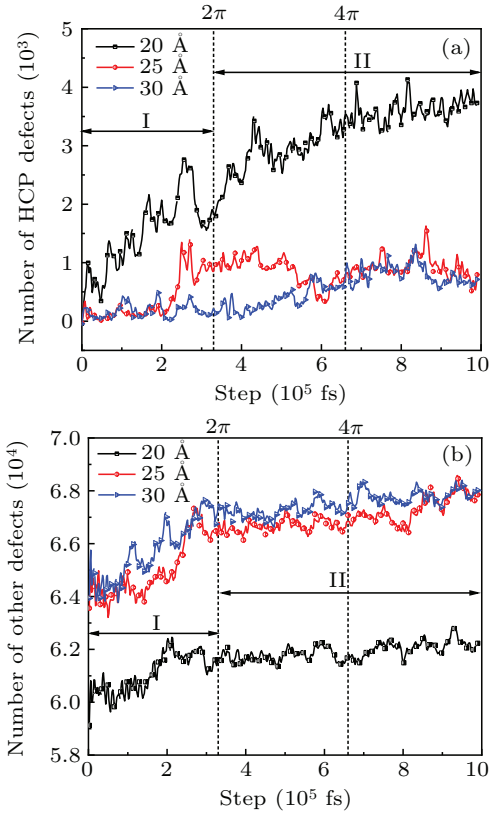


Fig. 21. Dynamic response curves of atomic number of partial defects *versus* time steps at different distances between strengthening phase and friction surface: (a) dynamic response curve of HCP defect atom number *versus* time steps and (b) dynamic response curve of other defect atom number *versus* time steps.

4. Conclusions

In this work, the nano-friction behavior of WC/Cu composites by repeated friction of diamond grinding balls is investigated by using the MD simulation method. The conclusions are summarized as follows.

(i) The changes of friction force, friction coefficient, and abrasion depth are divided into two phases, *i.e.*, the first friction with the three amplitude fluctuations, which is relatively gentle, and the repeated friction, where the amplitude fluctuations gradually become larger, and the peak appears near the WC phase, which is related to the distance between the strengthening phase WC and the friction surface. The smaller the distance between the strengthening phase and the initial friction surface, the more obvious the strengthening effect of WC on the matrix Cu. When the grinding ball moves to the front end of the WC phase, the local stress is highly concentrated and a large number of dislocations are generated inside the workpiece. In addition, dislocation plugging is formed under the blockage of the WC phase, which makes the region strengthened. During the initial friction, the number of HCP and other structure atoms increase faster, whereas, during re-

peated friction, the number of HCP and ther structure atoms increase slower. Meanwhile, there is less debris accumulated near the WC phase, while there is more debris accumulated at the position without the WC phase. It shows that the presence of the WC phase makes the material in its vicinity unable to be removed easily.

(ii) During initial friction, the amount of material removed is larger, and more atoms undergo lattice deformation, with a continuously increasing total energy, during repeated friction the amount of material removed is smaller, and fewer atoms undergo lattice deformation, the change of the total energy becomes flat. At the same time, the valleys appearing near the WC phase indicates that a large number of dislocations and defects are formed near the WC phase accompanied with the consuming energy, leading the energy values to lie in the valleys.

(iii) As the distance between the WC phase and the initial friction surface increases, the friction force decreases the friction coefficient also decreases without larger fluctuations, and the wear mark depth gradually increases but the amplitude decreases near the WC phase. In addition, the distance between the WC phase and the initial friction surface is greater than 20 Å, producing fewer HCP defect atoms and more other atoms. It shows that the strengthening effect gradually decreases until it disappears when the distance of the WC phase from the initial friction surface is larger than 20 Å.

Acknowledgements

Project supported by the National Natural Science Foundation of China (Grant No. 52005236) and the Natural Science Foundation of Gansu Province, China (Grant No. 20JR5RA442).

References

[1] Zhai W Z, Bai L C, Zhou R H, Fan X L, Kang G Z, Liu Y and Zhou K 2021 *Adv. Sci.* **8** 2003739
[2] Holmberg K and Erdemir A 2017 *Friction* **5** 263
[3] Dang C, Liu H M, Feng S, Qu Y, Hu Q L and Jiang J C 2019 *Mater. Res. Express* **6** 106312
[4] Wang C Z, Gan X P, Tao J M, Xie M, Yi J H and Liu Y C 2019 *Nanotechnology* **31** 045701
[5] Xu X Z, Yi D, Wang Z C, Yu J C, Zhang Z H, Qiao R X, Sun Z H, Hu Z H, Gao P and Peng H L 2018 *Adv. Mater.* **30** 1702944
[6] Arnaud C, Lecouturier F, Mesguich D, Ferreira N, Chevallier G, Estournès C, Weibel A and Laurent C 2016 *Carbon* **96** 212
[7] Baig Z, Mamat O and Mustapha M 2018 *Crit. Rev. Solid State Mater. Sci.* **43** 1
[8] Fan T X, Liu Y, Yang K M, Song J and Zhang D 2018 *Acta Metall. Sin.* **55** 16
[9] Zheng M, Qu D F, Wei X C, Zhang Z, Zhu Z X, Wang L J and Chen W H 2022 *Appl. Phys. A* **128** 1
[10] Tsakiris V, Enescu E, Radulian A, Lucaci M, Lungu M, Mocioi N, Leonat L, Cirstea D and Caramitu A 2016 *International Symposium on Fundamentals of Electrical Engineering (ISFEE)*, 30 June–02 July Bucharest, Romania, p. 1–6
[11] Zhai H X and Huang Z 2004 *Wear* **257** 414
[12] Aida H, Doi T, Takeda H, Katakura H, Kim S W, Koyama K, Yamazaki T and Uneda M 2012 *Curr. Appl Phys.* **12** S41
[13] Goel S, Kovalchenko A, Stukowski A and Cross G 2016 *Acta Mater.* **105** 464
[14] Zhang L C and Tanaka H 1998 *Tribol. Int.* **31** 425
[15] Shabani M, Paydar M H, Zamiri R, Goodarzi M and Moshksar M M 2016 *J. Mater. Res. Technol.* **5** 5
[16] Wei K X, Zhou H R, Jia F L, Zhang K, Wei W, Chu F Q, Wang D D and Alexandrov I V 2021 *Surf. Interfaces* **24** 101142
[17] Freschi M, Di Virgilio M, Zanardi G, Mariani M, Lecis N and Dotelli G 2021 *Lubricants* **9** 53
[18] Li X H, Yan S J, Chen X, Hong Q H and Wang N 2020 *J. Alloys Compd.* **834** 155182
[19] Chen L, Hou Z C, Liu Y F, Luan C, Zhu L and Li W Z 2020 *Composites, Part A* **138** 106063
[20] Bahador A, Umeda J, Hamzah E, Yusof F, Li X C and Kondoh K 2020 *Mater. Sci. Eng., A* **772** 138797
[21] Zhang C, Lu C, Pei L Q, Li J Q and Wang R 2020 *Composites, Part B* **182** 107610
[22] Song H Y, Duan B B, Wang Y J, An M and Li Y L 2020 *Mater. Chem. Phys.* **253** 123254
[23] Peng W X, Sun K, Abdullah R, Zhang M, Chen J and Shi J Q 2019 *Appl. Surf. Sci.* **487** 22
[24] Feng Q, Song X Y, Xie H X, Wang H B, Liu X M and Yin F X 2017 *Mater. Des.* **120** 193
[25] Zhu J D, Liu X, Zhou X D and Yang Q S 2021 *Comput. Mater. Sci* **188** 110179
[26] Hosseini S V and Vahdati M 2012 *Comput. Mater. Sci* **65** 29
[27] Xu F F, Fang F Z and Zhang X D 2018 *Comput. Mater. Sci* **143** 133
[28] Zhu Z X, Peng B, Feng R C, Wang L J, Jiao S and Dong Y 2019 *Sci. China Technol. Sci.* **62** 1916
[29] Li J, Fang Q H, Liu B and Liu Y W 2016 *Appl. Surf. Sci.* **384** 419
[30] Swope W C, Andersen H C, Berens P H and Wilson K R 1982 *J. Chem. Phys.* **76** 637
[31] Zhu Z X, Wang H, Qiang Z X, Jiao S, Wang L J, Zheng M, Zhu S Y, Cheng J and Yang J 2021 *Coatings* **11** 896
[32] Fang Q H, Wang Q, Li J, Zeng X and Liu Y W 2017 *RSC Adv.* **7** 42047
[33] Juslin N, Erhart P, Träskelin P, Nord J, Henriksson K O, Nordlund K, Salonen E and Albe K 2005 *J. Appl. Phys.* **98** 123520
[34] Imran M, Hussain F, Rashid M and Ahmad S 2012 *Chin. Phys. B* **21** 126802
[35] Yin Z H, Zhu P Z and Li B Z 2021 *Tribol. Lett.* **69** 38
[36] Wei W, Chen L, Gong H R and Fan J L 2019 *J. Phys.: Condens. Matter* **31** 305002
[37] Imran M, Hussain F, Rashid M and Ahmad S 2012 *Chin. Phys. B* **21** 116201
[38] Zhang R, Kong L, Gong H and Liu B 2004 *J. Phys.: Condens. Matter* **16** 5251
[39] Tersoff J 1989 *Phys. Rev. B* **39** 5566
[40] Ye Y, Biswas R, Morris J, Bastawros A and Chandra A 2003 *Nanotechnology* **14** 390
[41] Archard J 1953 *J. Appl. Phys.* **24** 981
[42] Khosravi J, Givi M K B, Barmouz M and Rahi A 2014 *Int. J. Adv. Manuf. Tech.* **74** 1087
[43] Doan D Q, Fang T H, Tran A S and Chen T H 2019 *Comput. Mater. Sci* **170** 109162
[44] Stukowski A, Bulatov V V and Arsenlis A 2012 *Modell. Simul. Mater. Sci. Eng.* **20** 085007
[45] Yin Z, Zhu P and Li B 2021 *Tribol. Lett.* **69** 1
[46] Zhang Z B and Urbassek H M 2018 *Comput. Mater. Sci* **145** 109
[47] Wang J P, Liang J W, Wen Z X, Yue Z F and Peng Y 2022 *Mech. Mater.* 104204